Synthesis of Zinc-Nitrogen-Codoped Zirco-Titania Composite (Zn-N-Codoped ZT) as a Photocatalyst for Photodegradation of Phenol Under Visible Light Irradiation

Nadya Putri Utami[1], Rian Kurniawan[1,2], Mokhammad Fajar Pradipta[1], and Akhmad Syoufian[1*]

[1]*Department of Chemistry, Faculty of Mathematics and Natural Sciences, Universitas Gadjah Mada, Sekip Utara, Yogyakarta 55281, Indonesia*

[2]*Institute of Chemical Technology, Universität Leipzig, Linnéstr. 3, Leipzig 04103, Germany*

*** Corresponding author:**

email: akhmadsyoufian@ugm.ac.id

Received: November 13, 2024
Accepted: January 19, 2025

DOI: 10.22146/ijc.101519

Abstract: *Zinc (Zn) and nitrogen (N) were introduced as codopants in zirco-titania (Zn-N-codoped ZT) composite photocatalyst. This research primarily aimed to investigate the codoping effect of Zn and N in ZT composite for the photodegradation of phenol under visible light irradiation. The composite was prepared through the sol-gel method, where a suspension of ZrO_2 mixed with Zn dopant (w_{Zn}/w_{Ti} = 1–9%) and N dopant (w_N/w_{Ti} = 10%) was added dropwise to TTIP in ethanol solution. Calcination was conducted at the temperature of 500, 700, and 900 °C. FTIR shows an increasing absorbance at 1095 cm^{-1} as the increasing Zn up to 5%. XRD reveals that Zn-N cooping influences anatase and rutile crystallization above 700 °C. SEM-EDX of 5Zn-N-ZT-500 displays a spherical and homogeneous morphology. Photodegradation of 10 mg L^{-1} phenol solution under visible light irradiation was conducted to evaluate the photocatalytic activity. The composite with 5% Zn and 10% N calcined at 900 °C achieved the lowest band gap of 2.90 eV. The highest phenol degradation percentage after 120 min irradiation, 51.96%, was attained by the composite containing 5% Ni and 10% N calcined at 500 °C (k_{obs} = 8.4 × 10^{-3} min^{-1}).*

Keywords: *codoping; phenol; photodegradation; Zn-N-codoped ZT*

■ INTRODUCTION

Industrial waste, such as phenol, contributes to water pollution and has adverse environmental effects [1]. Phenol, a harmful organic compound, is produced by industries involved in coal gasification, paper manufacturing, petroleum, paint, and textiles [2]. It is known for its toxicity and potential to cause teratogenic and carcinogenic effects in living organisms [3]. Phenol levels can be reduced through physical methods (like activated carbon adsorption), chemical methods (such as solvent extraction), and biological methods (including aerobic and anaerobic processes) [1]. However, these techniques often involve lengthy processes, high costs, low efficiency, and generating secondary waste [2].

The photocatalytic approach is recognized for its effectiveness in breaking down pollutants without generating additional waste that could damage the environment [4]. This method offers benefits such as rapid processing, low cost, and efficient removal of toxicity [5]. Light energy is necessary to excite the photocatalyst during photocatalysis, producing charged carriers essential for the degradation process. Electrons or holes trigger the formation of radical species like superoxide radicals ($\bullet O_2^-$). These radicals react with water to form hydroxyl ions (OH^-), which then interact with holes (h^+) to generate hydroxyl radicals ($\bullet OH$). The hydroxyl radicals decompose phenol compounds into simpler substances, such as CO_2 and H_2O [6-8]. The mechanism of photodegradation of organic compounds by a photocatalyst (not balanced) can be explained as follows [9-11].

$$\text{photocatalyst} + h\nu\ (\text{photon}) = e^-_{CB} + h^+_{VB}$$

$$e^-_{CB} + O_2 \rightarrow O_2^-$$

$$\bullet O_2^- + H_2O \rightarrow \bullet OH + HO^-$$

$$h^+_{VB} + H_2O \rightarrow \bullet OH + H^+$$

$$\text{phenol compound} + {\bullet}OH \rightarrow CO_2 + H_2O$$

A photocatalyst is a photoactive substance that utilizes photons to drive a chemical reaction [12]. Materials like TiO_2 serve as photocatalysts due to their properties as non-toxic, inert, thermally and chemically stable, affordable semiconductors that enhance the oxidation of various organic compounds and demonstrate high photocatalytic efficiency [13-16]. TiO_2 exists in three structural forms: rutile, anatase, and brookite. The rutile and anatase phases have a band gap of 3.0 and 3.2 eV, respectively [15]. Among these, the anatase phase exhibits superior photocatalytic performance compared to rutile [17]. The anatase phase has a superior ability to trap holes and a lower recombination rate than the rutile phase [18]. TiO_2 primarily absorbs UV light (< 400 nm) [19], while UV radiation constitutes only 5–7% of sunlight, and visible light accounts for 46% [6]. To extend the photocatalytic activity of TiO_2 into the visible range, TiO_2 can be doped with metals and nonmetals [20], broadening its absorption spectrum to include visible light [21-22].

Dopants used in photocatalysts include nonmetals such as N [23], C [24], and S [25], as well as transition metals like Fe [17], Co [26], Cr [27], Cu [28], Mo [29], Zn [30], and Ta [15]. These dopants are effective in reducing the rate of electron-hole recombination and decreasing the band gap energy [15]. Codoping has a synergistic effect on enhancing the performance of TiO_2 under visible light by creating new energy levels from the dopants, which can narrow the band gap of TiO_2 [31]. Nonmetal dopants create mid-energy levels above the valence band (VB), whereas metal dopants establish energy levels below the conduction band (CB) [32]. TiO_2 photocatalysts doped with Zn and N may experience a phase transformation from the anatase to the rutile phase at a temperature of 550 °C [33-35]. This phase transformation can be mitigated by combining TiO_2 with other semiconductors such as SnO_2, WO_2, ZrO_2, CeO_2, CdS, and Fe_2O_3 [36-38].

ZrO_2 exists in three polymorphic crystal phases: cubic phase is stable above 2370 °C, tetragonal is stable between 1170–2370 °C, and monoclinic is stable below 1170 °C [39]. ZrO_2 is selected for its role as a support material and active host that helps prevent the phase transition of TiO_2 from anatase to rutile. The resulting ZrO_2-TiO_2 (ZT) composite benefits from high thermal stability, reduced electron-hole recombination, increased surface area, and improved photocatalytic activity under visible light [30,40-41]. Moreover, the ZT composite can create a heterojunction, where a junction develops between TiO_2 and ZrO_2, which helps lower the recombination rate [42] since electrons and holes from ZrO_2 can be transferred to the CB and VB of TiO_2. The movement of electrons from trap states or the CB of ZrO_2 to the CB of TiO_2 enhances the availability of free electrons for the reduction process [33,42]. Meanwhile, holes move from the VB of ZrO_2 to the VB of TiO_2, where they can initiate the oxidation reaction [33].

The photocatalytic degradation of phenol solution under visible light was conducted using a Zn-N-codoped ZT composite (Zn-N-ZT). TiO_2 codoped with Zn and N was grown on the surface of ZrO_2 through a sol-gel process. The concentration of the Zn dopant was varied while keeping the concentration of the nitrogen dopant constant, resulting in different Zn levels in the Zn-N-ZT composites. The calcination temperature was varied to assess its impact on the crystal phase and size. Additionally, the irradiation time was varied to evaluate its effect on the extent of phenol degradation. Consequently, the Zn-N-ZT material is anticipated to respond well to visible light and efficiently degrade the phenol solution.

■ EXPERIMENTAL SECTION

Materials

Titanium(IV) tetraisopropoxide (TTIP, 97%) as TiO_2 precursor was obtained from Sigma-Aldrich and zirconia (ZrO_2) powder was obtained from Jiaozuo Huasu. Urea ($CO(NH_2)_2$, Merck) and zinc nitrate hexahydrate ($Zn(NO_3)_2{\cdot}6H_2O$, 99%, Merck) were both selected as the sources of dopant. Ethanol (99%, Merck) and distilled water (Jaya Sentosa) were used as solvents. Phenol as the target compound was obtained from Merck.

Instrumentation

The vibrational spectra of the composite's functional groups were identified using a Fouriertransform infrared (FTIR) Thermo Nicolet iS10, covering a range of 400 to 4000 cm^{-1}. The crystalline structure of the materials was analyzed with an X-ray diffractometer (XRD) PANalytical X'Pert PRO MRD, utilizing Cu Kα radiation (λ = 1.54 Å, 40 kV, 30 mA). Crystal size (L) was determined using the Scherrer equation (Eq. (1)) [43];

$$L = \frac{0.9\lambda}{B\cos\theta} \quad (1)$$

where λ is the X-ray wavelength, θ is the Bragg angle, and B is half the full width of the maximum intensity of the peak in radians. The morphology and elemental composition of the photocatalyst were characterized by a scanning electron microscope energy dispersive X-ray spectrometer (SEM-EDX) JEOL-JSM 6510 LA series with an accelerating voltage of 20 kV. Specular reflectance UV-vis spectrometer UV 1700 Pharmaspec (SR-UV) was used to measure the absorption spectra in the wavelength range of 200–800 nm and to determine the composite's band gap energy using the absorption edge shift method (Eq. (2)) [44];

$$E_g = \frac{1240}{\lambda_g} \quad (2)$$

where E_g is the band gap energy (eV) and λ_g represents the absorbance edge value obtained from the intersection point between two linear equations at which the absorbance increases. Photocatalytic activity tests for phenol solution degradation were conducted under visible light from a LIFE MAX 30W/765 PHILIPS TLD lamp. The phenol concentration after degradation was measured at a maximum wavelength of 269 nm using a UV-1800 Shimadzu UV-vis spectrophotometer.

Procedure

Preparation of Zn-N-codoped ZT composites

The Zn-N-ZT composite was synthesized using a sol-gel method. Initially, 2.5 mL of TTIP was dissolved in 25 mL of absolute ethanol. Separately, 1.0 g of ZrO_2 powder and 86.8 mg of urea (w_N/w_{Ti} = 10%) were dispersed in 10 mL of demineralized water, along with various amounts of $Zn(NO_3)_2{\cdot}6H_2O$ aimed to be 1.0, 3.0, 5.0, 7.0, and 9.0% (w_{Zn}/w_{Ti}). This suspension was added dropwise to the TTIP solution and stirred for 30 min. The resulting mixture was centrifuged for 30 min at 2000 rpm to separate the solid. Afterwards, the solid was filtered, air-dried for 24 h, and then oven-dried at 80 °C for another 24 h. The solid was calcined at 500, 700, and 900 °C for 4 h. The composites were designated as αZn-N-ZT-β, where α represents the percentage of Zn as a dopant and β denotes the calcination temperature (°C). All samples were characterized using XRD, FTIR, SR-UV, and SEM-EDX.

Photodegradation test of phenol using Zn-N-codoped ZT composites

The Zn-N-ZT composite photocatalyst (100 mg) was introduced into 100 mL of a 10 mg L^{-1} phenol (Ph) solution. The mixture was stirred for 15 min before being exposed to visible light, allowing the adsorption of Ph to reach equilibrium. It was then continuously stirred and irradiated for 15, 30, 45, 60, 75, 90, 105, and 120 min using a LIFE MAX 30W/765 PHILIPS TLD lamp. After irradiation, the photocatalyst was separated from the solution by centrifugation at 3000 rpm for 30 min. The Ph concentration following photodegradation was assessed by measuring the absorbance at 269 nm. To obtain a reliable result, the photodegradation experiments were repeated three times for each material. The photodegradation kinetics of the Ph solution were analyzed using a pseudo-first-order Langmuir-Hinshelwood model (Eq. (3) and (4));

$$-\frac{dC}{dT} = k_{obs}C \quad (3)$$

$$\ln C = -k_{obs}t + \ln C_0 \quad (4)$$

where C represents the phenol concentration at time t, C_0 is the initial concentration, t is the irradiation time, and k_{obs} is the observed rate constant. The percentage of Ph degradation was determined using Eq. (5);

$$\%\text{pH degradation} = \frac{C_i - C_f}{C_i} \times 100\% \quad (5)$$

where C_i and C_f denote the initial and final concentrations of Ph, respectively.

■ RESULTS AND DISCUSSION

The FTIR spectra for the Zn-N-ZT-500 composite with different Zn concentrations, along with TiO_2, ZrO_2, and N-ZT-500, are presented in Fig. 1(a–h). Absorption in the 400–700 cm^{-1} range corresponds to the stretching

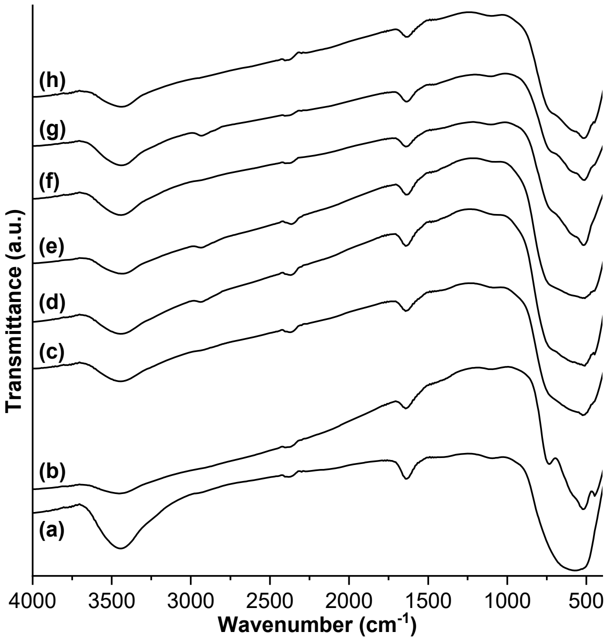

Fig 1. FTIR spectra of (a) TiO_2, (b) ZrO_2, (c) N-ZT-500, (d) 1Zn-, (e) 3Zn-, (f) 5Zn-, (g) 7Zn-, and (h) 9Zn-N-ZT-500

vibrations of Zr–O and Ti–O bonds [42]. The monoclinic phase of ZrO_2 is identified in the 450–650 cm^{-1} range [45]. The absorption at 1095 cm^{-1} is attributed to the vibrations of Zn–O–Zr [46] or Zn–O–Ti bonds or both [30,47]. The intensity of this peak sharpens as the Zn dopant concentration increases up to 5% Zn, likely due to the incorporation of excess Zn into interstitial sites or its agglomeration [48]. Peaks at 1600 and 3400–3500 cm^{-1} are associated with the bending vibration of the H–O–H group and the stretching vibration of the O–H group, indicating the presence of remaining water molecules in the composite surface during synthesis [46,49].

Fig. 2(a–c) displays the FTIR spectra of 5Zn-N-ZT with varying calcination temperatures. As the calcination temperature rises from 500 to 900 °C, the intensity at 1600 and 3400–3500 cm^{-1} decreases, reflecting the reduction of water molecules on the composite surface [20]. Additionally, the intensity at 1095 cm^{-1} diminishes as higher temperatures cause dopants to agglomerate [50]. At the wavenumber around 500 cm^{-1}, the absorption peak becomes flatter with increasing calcination temperature due to the phase transition of TiO_2 from anatase to rutile. This transition alters the Ti-O-Ti bond length, affecting the vibrational absorption energy [40].

Fig. 3 displays the XRD results for the Zn-N-ZT-500 composites with varying concentrations of Zn dopant alongside the diffraction patterns of TiO_2, ZrO_2, and N-ZT materials for comparison. The diffraction patterns indicate that pure ZrO_2 shows peaks at 2θ of 28° (d_{-111}) and 31° (d_{111}), which correspond to the monoclinic phase (00-036-0420) [26]. In contrast, pure

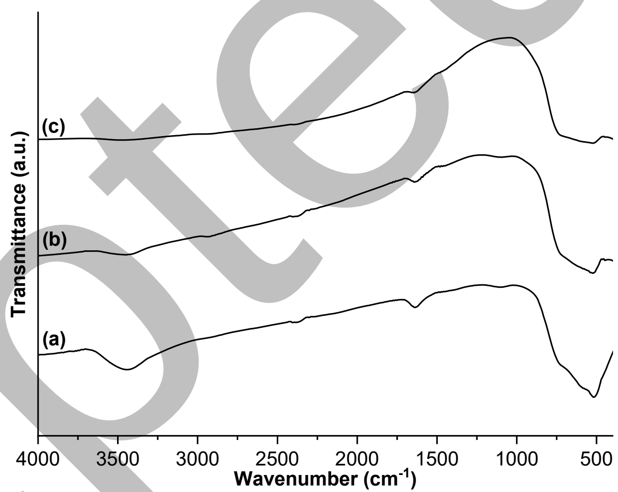

Fig 2. FTIR spectra of 5Zn-N-ZT at (a) 500, (b) 700, and (c) 900 °C

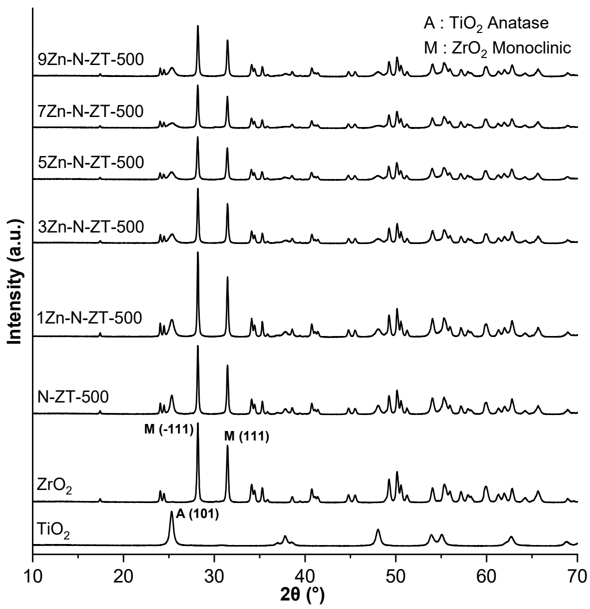

Fig 3. XRD patterns of Zn-N-ZT-500 composite with various Zn concentrations

TiO_2 exhibits major peaks at 2θ of 25° (d_{101}), indicative of the anatase phase (00-021-1272) [17]. The Debye-Scherrer equation [43] was used to calculate the average crystallite size of Zn-N-ZT, with results summarized in Table 1. Peaks for anatase at 2θ = 25° (d_{101}) and monoclinic at 2θ = 28° (d_{-111}) were used to determine these sizes.

The monoclinic intensity decreases up to a Zn concentration of 5% and then increases again at 7% Zn. The anatase intensity decreases with increasing Zn concentration up to 5% (the optimum concentration). Zn dopant acts as an impurity and causes crystal defects during calcination because Zn enters the crystal structure of ZT composites during the rearrangement process [51]. The Zn-N-ZT composite has a smaller crystallite size for anatase and monoclinic phases compared to its parent materials (ZrO_2 and TiO_2) because Zn and N dopants were successfully doped into the composite lattice surface [43]. The crystallite size of Zn-N-ZT (anatase and monoclinic) decreases from 1 to 5% Zn concentration and increases again after the addition of 7% Zn. The reduction in crystallite size is due to crystal defects originating from the Zn^{2+} dopant added to the Zr–O–Zr or Ti–O–Ti network, where Zr^{4+} or Ti^{4+} positions are replaced by Zn^{2+} ions [21,52]. This substitution occurs due to the difference in ionic size and valence between Zn cations and Zr or Ti cations, where the ionic radius of Zn^{2+} is smaller than that of Zr^{4+} or Ti^{4+} [53]. Crystal defects may occur due to oxygen vacancies in the crystal structure [22]. The increase in crystallite size of anatase and monoclinic phases at 7% Zn is because the amount of dopant exceeds the optimum limit, leading to dopant agglomeration on the crystal surface [23].

The XRD patterns of the 5Zn-N-ZT composite at different calcination temperatures are shown in Fig. 4. After calcination at 700 °C, 5Zn-N-ZT reveals a rutile phase diffraction pattern (ICDD: 00-021-1276) at 27° (d_{110}) [41]. The anatase phase is still visible at calcination temperatures of 700 °C but with lower intensity compared to the 500 °C calcination temperature. This indicates ZrO_2 acting as a supporting material that can inhibit the phase transformation of anatase to rutile in TiO_2 [54]. The crystallinity of the 5Zn-N-ZT composite increases with the

Table 1. The average crystallite size of various Zn-N-ZT composite

Material	Crystal phase	L (nm)
TiO_2	Anatase	59
ZrO_2	Monoclinic	46
N-ZT-500	Anatase	30
	Monoclinic	46
1Zn-N-ZT-500	Anatase	41
	Monoclinic	52
3Zn-N-ZT-500	Anatase	17
	Monoclinic	52
5Zn-N-ZT-500	Anatase	19
	Monoclinic	46
5Zn-N-ZT-700	Anatase	41
	Rutile	59
	Monoclinic	52
5Zn-N-ZT-900	Rutile	59
	Monoclinic	52
7Zn-N-ZT-500	Anatase	26
	Monoclinic	46
9Zn-N-ZT-500	Anatase	15
	Monoclinic	46

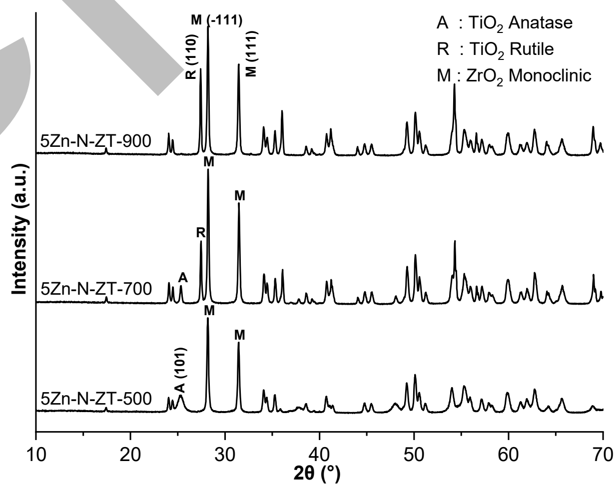

Fig 4. XRD patterns of 5Zn-N-ZT composite calcined at various temperatures

rise in calcination temperature because of the improved atomic order in the crystal as the calcination temperature increases [55–57]. According to the analysis, the crystallite size of the anatase phase increased as the calcination temperature rose from 500 to 700 °C [58] and was undetectable at 900 °C [59]. The rutile phase began to emerge at 700 °C [34,60], while the crystallite size of the rutile phase remained unchanged at calcination temperatures of 700 and 900 °C. The crystallite size of the monoclinic phase in 5Zn-N-ZT increased from 500 to 700 °C [61] due to the more stable growth of ZT crystals [20]. However, from 700 to 900 °C, there was no change in the monoclinic crystallite size. This stagnation in crystallite size is attributed to particle agglomeration at elevated calcination temperatures [62-63]. Agglomeration inhibits the optimal integration of the dopant into the crystal lattice [64].

The SEM images of ZrO_2 and 5Zn-N-ZT-500 composite are shown in Fig. 5(a–c), alongside the elemental mapping of 5Zn-N-ZT-500. The ZrO_2 and 5Zn-N-ZT-500 composite exhibit a spherical and homogeneous morphology. The surface of ZrO_2 is smoother than the 5Zn-N-ZT-500 composite because the dopants undergo agglomeration due to the calcination temperature [65]. The elemental mapping of 5Zn-N-ZT-500 shows the evenly distributed Zr and Ti on the surface of the observed particles and confirms the formation of a composite instead of a mixture. Moreover, the presence of Zn appears to be homogeneous on the surface of composites, which also confirms the doping of Zn. The elemental mass percentage of ZrO_2 and 5Zn-N-ZT-500 measured by EDX analysis are displayed in Table 2. The small mass percentages of Zn and N indicate that both dopants were successfully doped into the 5Zn-N-ZT-500 composite. Dopants with a low mass percentage can prevent the

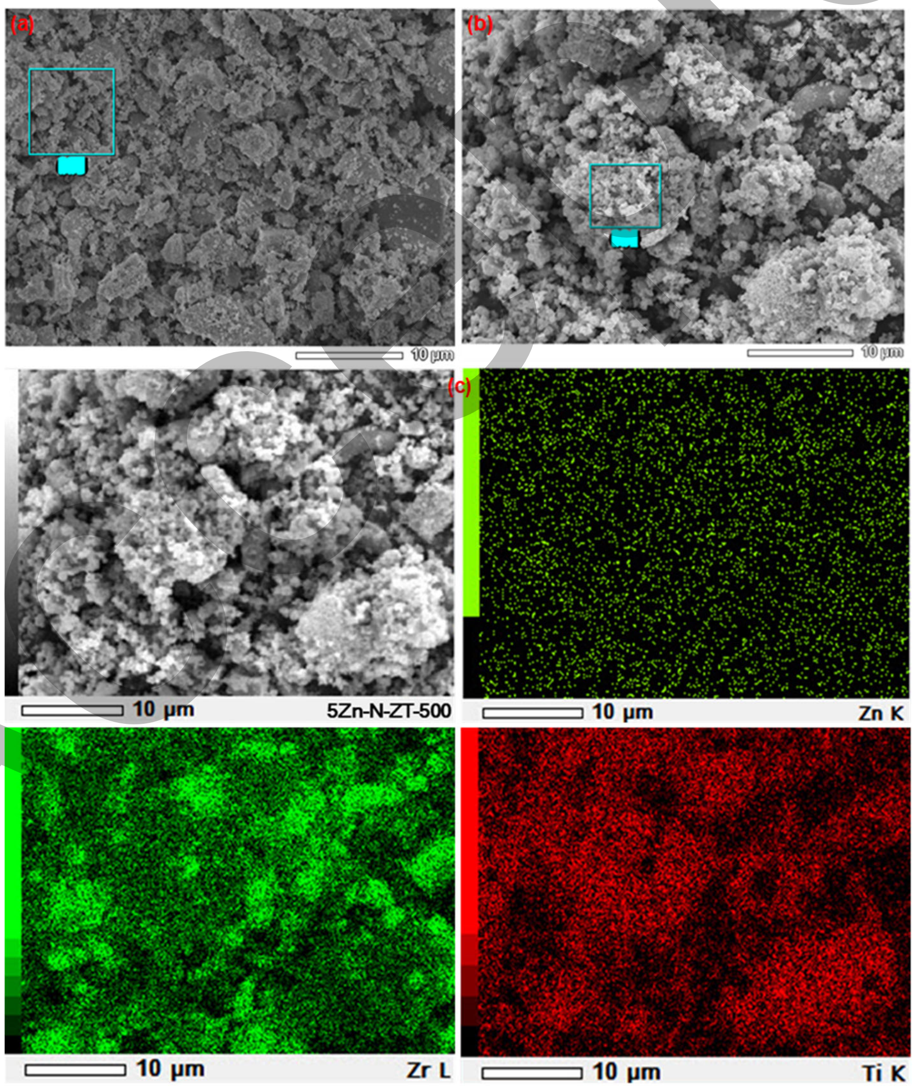

Fig 5. SEM images of (a) ZrO_2 and (b) 5Zn-N-ZT-500, and (c) elemental mapping of 5Zn-N-ZT-500

Table 2. EDX analysis of ZrO_2 and 5Zn-N-ZT-500

Material	%Mass					
	Zr	O	Ti	N	Zn	Total
ZrO_2	78.29	21.71	-	-	-	100
5Zn-N-ZT-500	15.44	43.22	35.63	2.68	3.03	100

formation of recombination centers and impact the structure and activity of the photocatalyst [66]. If the dopant concentration is excessively high, it can decrease photocatalytic efficiency [67]. Higher levels of dopants lead to the aggregation of dopant ions at specific sites, which causes the surface to accumulate charge [65].

The SRUV spectra of the Zn-N-ZT composite with varying Zn concentrations and calcination temperatures are depicted in Fig. 6(a). The band gap energy (E_g) was determined using the absorption edge method [44]. Fig. 6(b) shows the calculated E_g of the Zn-N-ZT composites. The E_g of all Zn-N-ZT materials are lower than that of TiO_2 (3.19 eV) and N-ZT-500 (3.18 eV) due to the codoping effect of Zn and N [4]. The presence of Zn and N dopants shifts the absorption edge towards the visible light region [21,68]. The E_g value of Zn-N-ZT-500 decreases with increasing Zn concentration up to 5%, then increases again at Zn concentrations up to 9% [30]. The increase in E_g is due to an excess amount of dopant, which leads to dopant agglomeration and weakens the doping effect [17,69]. The 5Zn-10N-ZT-500 composite shows the lowest E_g value of 3.06 eV with an absorption edge at the wavelength of 405 nm.

The spectra reveal a shift of the absorption edge towards longer wavelengths as the calcination temperature increases, indicating a decrease in E_g [43]. The lowest E_g value was observed at 5Zn-N-ZT-900, with a E_g of 2.90 eV and an absorption edge at 428 nm. The reduction of E_g is attributed to the transformation of anatase to rutile, with the rutile phase being more dominant in 5Zn-N-ZT-900 compared to the 5Zn-N-ZT-500 and 5Zn-N-ZT-700 composites. This observation aligns with the fact that the rutile phase has a smaller E_g compared to the anatase phase and that rutile has longer Ti–O–Ti bonds than anatase [48].

The photocatalytic performance of the Zn-N-ZT composite was assessed by testing its ability to degrade a Ph solution under visible light. The study varied the irradiation time and Zn concentration within the composite to identify the optimal conditions for Ph degradation. Ph concentration in the photodegraded samples was measured by absorbance at 269 nm. Fig. 7(a) illustrates the impact of irradiation time on Ph photodegradation using the Zn-N-ZT composite, while Fig. 7(b) presents the rate constant for Ph degradation. The 5Zn-N-ZT-500 composite demonstrated optimal

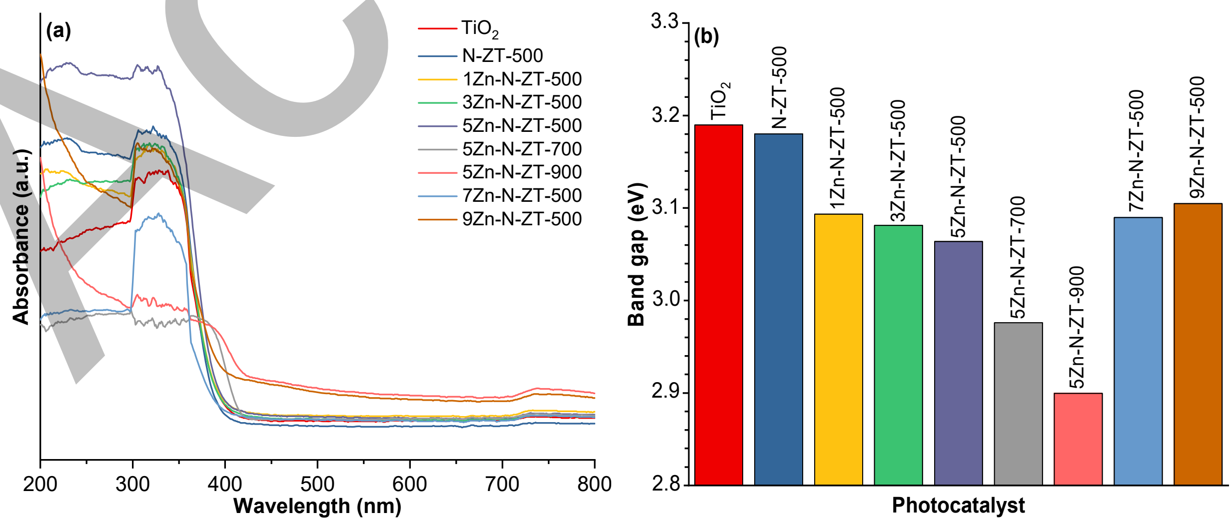

Fig 6. (a) SR-UV spectra and (b) band gap of various Zn-N-ZT composites

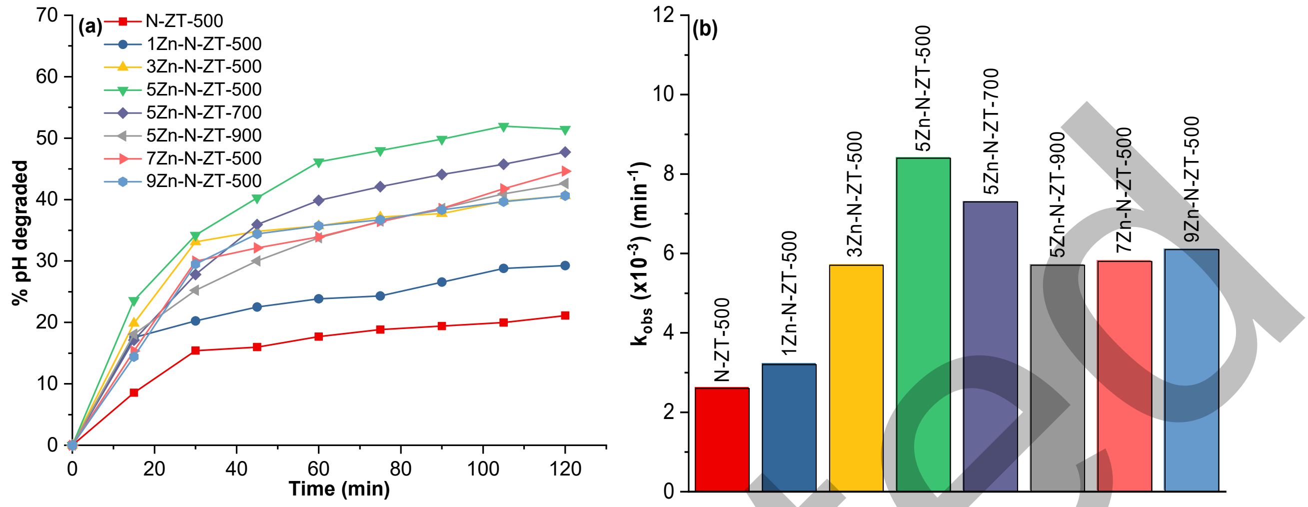

Fig 7. (a) Photodegradation of Ph over irradiation time and (b) observed rate constant k_{obs} of Ph photodegradation by various Zn-N-ZT composite

Ph degradation, achieving 51.96% degradation with an irradiation time of 105 min and k_{obs} of 8.4×10^{-3} min^{-1}, highlighting the enhancement of ZT's photocatalytic activity through Zn and N codoping.

The photocatalytic performance of a photocatalyst is closely tied to its electronic band structure, as a reduced band gap often diminishes redox power by either lowering the conduction band level, raising the valence band level, or both, which adversely affects photocatalytic efficiency [41]. Among the composites calcined at 500 °C with varying Zn concentrations, the 5Zn-N-ZT-500 material exhibits the highest photocatalytic activity and has the lowest band gap. XRD and SR-UV data suggest that even small amounts of dopants can significantly impact on the material photocatalytic performance. The decline in photocatalytic activity at Zn concentrations above 5% is likely due to the diminished effect of Zn codoping, as reflected in a higher band gap energy, which reduces the light absorption range, and the smaller average crystallite size of anatase, the active crystalline phase [70].

The percentage of photodegradation diminishes as the calcination temperature rises, with values of 51.96, 47.73, and 42.63% at temperatures of 500, 700, and 900 °C, respectively. This reduction is attributed to the phase transition of TiO_2 from anatase to rutile occurring at 700 and 900 °C [34]. However, the rutile phase has lower photocatalytic activity than the anatase phase [18]. When the photocatalyst is exposed to high-energy light, it forms h^+ in VB, a strong oxidant. The h^+ generates •OH radicals that break down phenol into simpler compounds [34]. Extended irradiation times allow the photocatalyst to absorb more photon energy, resulting in the generation of more •OH radicals [71], thereby enhancing the Ph degradation process.

CONCLUSION

The Zn-N-codoped zirco-titania composite photocatalyst was synthesized using the sol-gel method. FTIR analysis indicated that the Zn–O–Zr or Zn–O–Ti bonds or both vibrations at a wavenumber of 1095 cm^{-1} increased in intensity by adding up to 5% Zn dopant. Codoping with N and Zn, as well as coupling with ZrO_2, affects the crystallization of anatase and rutile at higher temperatures and inhibits the growth of TiO_2 crystals. Codoping with N and Zn reduces the Eg of the ZT composite to 2.90 eV (with 5% Zn, 10% N, and calcination at 900 °C). The Zn-N-codoped ZT photocatalyst with 5% Zn and 10% N calcined at 500 °C was able to degrade a 10 mg L^{-1} phenol solution by up to 51.96% after 105 min of visible light irradiation, with observed k_{obs} of 8.4×10^{-3} min^{-1}. Codoping of Zn and N enhances the photocatalytic performance of ZT under visible irradiation, and it becomes a highly potential photocatalyst to utilize sunlight for environmental remediation.

■ ACKNOWLEDGMENTS

Akhmad Syoufian is grateful for partial funding support provided by 2451/UN1/FMIPA.1.3/KP/PT.01.03/2024 Grant from The Faculty of Mathematics and Natural Sciences Universitas Gadjah Mada Indonesia.

■ CONFLICT OF INTEREST

All authors certify that they have no affiliations with or involvement in any organization or entity with any financial interest or non-financial interest in the subject matter or materials discussed in this manuscript.

■ AUTHOR CONTRIBUTIONS

Nadya Putri Utami served as the first author, collecting data, writing the initial draft, and performing revisions. Rian Kurniawan and Mokhammad Fajar Pradipta, served as co-authors, checked revision results, and provided suggestion for improvements to the written report. Akhmad Syoufian served as corresponding author, research supervisor, checked revision results, provided suggestion for improvements, and conducted final assessments of the data and the written report.

■ REFERENCES

[1] Chen, X., Guo, R., Pan, W., Yuan, Y., Hu, X., Bi, Z., and Wang, J., 2022, A novel double S-scheme photocatalyst $Bi_7O_9I_3/Cd_{0.5}Zn_{0.5}S$ QDs/WO_{3-x} with efficient full-spectrum-induced phenol photodegradation, *Appl. Catal., B*, 318, 121839.

[2] Prabha, I., and Lathasree, S., 2014, Photodegradation of phenol by zinc oxide, titania and zinc oxide-titania composites: Nanoparticle synthesis, characterization and comparative photocatalytic efficiencies, *Mater. Sci. Semicond. Process.*, 26, 603–613.

[3] Xue, Y., Zhong, H., Liu, B., Zhao, R., Ma, J., Chen, Z., Li, K., and Zuo, X., 2022, Colorimetric sensing strategy for detection of cysteine, phenol cysteine, and phenol based on synergistic doping of multiple heteroatoms into sponge-like Fe/NPC nanozymes, *Anal. Bioanal. Chem.*, 414 (14), 4217–4225.

[4] Li, H., Bharti, B., Manikandan, V., AlSalhi, M.S., Asemi, N.N., Wang, Y., Jin, W., and Ouyang, F., 2023, Nitrogen–fluorine co-doped TiO_2/SiO_2 nanoparticles for the photocatalytic degradation of acrylonitrile: Deactivation and regeneration, *Chemosphere*, 340, 139986.

[5] Krishnan, A., Swarnalal, A., Das, D., Krishnan, M., Saji, V.S., and Shibli, S.M.A., 2024, A review on transition metal oxides based photocatalysts for degradation of synthetic organic pollutants, *J. Environ. Sci.*, 139, 389–417.

[6] Rehman, G.U., Tahir, M., Goh, P.S., Ismail, A.F., Hafeez, A., and Khan, I.U., 2021, Enhancing the photodegradation of phenol using Fe_3O_4/SiO_2 binary nanocomposite mediated by silane agent, *J. Phys. Chem. Solids*, 153, 110022.

[7] Bharali, D., Saikia, S., Devi, R., Choudary, B.M., Gour, N.K., and Deka, R.C., 2023, Photocatalytic degradation of phenol and its derivatives over ZnFe layered double hydroxide, *J. Photochem. Photobiol., A*, 438, 114509.

[8] Qi, K., Wang, Z., Xie, X., and Wang, Z., 2023, Photocatalytic performance of pyrochar and hydrochar in heterojunction photocatalyst for organic pollutants degradation: Activity comparison and mechanism insight, *Chem. Eng. J.*, 467, 143424.

[9] Samarasinghe, L.V., Muthukumaran, S., and Baskaran, K., 2024, Recent advances in visible light-activated photocatalysts for degradation of dyes: A comprehensive review, *Chemosphere*, 349, 140818.

[10] Mohamed, A., Yousef, S., Nasser, W.S., Osman, T.A., Knebel, A., Sánchez, E.P.V., and Hashem, T., 2020, Rapid photocatalytic degradation of phenol from water using composite nanofibers under UV, *Environ. Sci. Eur.*, 32 (1), 160.

[11] Grosu, E.F., Cârja, G., and Froidevaux, R., 2018, Development of horseradish peroxidase/layered double hydroxide hybrid catalysis for phenol degradation, *Res. Chem. Intermed.*, 44 (12), 7731–7752.

[12] Samriti, S., Tyagi, R., Ruzimuradov, O., and Prakash, J., 2023, Fabrication methods and mechanisms for designing highly-efficient photocatalysts for energy and environmental applications, *Mater. Chem. Phys.*, 307, 128108.

[13] Ramamoorthy, S., Das, S., Balan, R., and Lekshmi,

I.C., 2021, TiO_2-ZrO_2 nanocomposite with tetragonal zirconia phase and photocatalytic degradation of Alizarin Yellow GG azo dye under natural sunlight, *Mater. Today: Proc.*, 47, 4641–4646.
[14] Yang, J., Liu, Z., Jing, J., Zhang, X., Fu, Y., Li, M., and Wang, H., 2024, Novel superhydrophobic sponge with flower-like architecture for oily emulsion separation and organic pollutants photodegradation, *J. Environ. Chem. Eng.*, 12 (3), 112680.
[15] Barrocas, B., Monteiro, O.C., Nunes, M.R., and Silvestre, A.J., 2019, Influence of Re and Ru doping on the structural, optical and photocatalytic properties of nanocrystalline TiO_2, *SN Appl. Sci.*, 1 (6), 556.
[16] Zhang, Z., Zhao, C., Duan, Y., Wang, C., Zhao, Z., Wang, H., and Gao, Y., 2020, Phosphorus-doped TiO_2 for visible light-driven oxidative coupling of benzyl amines and photodegradation of phenol, *Appl. Surf. Sci.*, 527, 146693.
[17] Hayati, R., Kurniawan, R., Prasetyo, N., Sudiono, S., and Syoufian, A., 2022, Codoping effect of nitrogen (N) to iron (Fe) doped zirconium titanate ($ZrTiO_4$) composite toward its visible light responsiveness as photocatalysts, *Indones. J. Chem.*, 22 (3), 692–702.
[18] Ajmal, A., Majeed, I., Malik, R.N., Idriss, H., and Nadeem, M.A., 2014, Principles and mechanisms of photocatalytic dye degradation on TiO_2 based photocatalysts: A comparative overview, *RSC Adv.*, 4 (70), 37003–37026.
[19] Aimeur, M., Baudu, M., Zermane, F., Joussein, E., and Bouras, O., 2021, Evaluation of the use of free or supported phenalenone based on natural halloysite for phenol photodegradation in aqueous solution, *J. Photochem. Photobiol., A*, 404, 112904.
[20] Van Thuan, D., Ngo, H.L., Thi, H.P., and Chu, T.T.H., 2023, Photodegradation of hazardous organic pollutants using titanium oxides-based photocatalytic: A review, *Environ. Res.*, 229, 116000.
[21] Rehman, S., Ullah, R., Butt, A.M., and Gohar, N.D., 2009, Strategies of making TiO_2 and ZnO visible light active, *J. Hazard. Mater.*, 170 (2-3), 560–569.
[22] Pirzada, B.M., Mir, N.A., Qutub, N., Mehraj, O., Sabir, S., and Muneer, M., 2015, Synthesis, characterization, and optimization of photocatalytic activity of TiO_2/ZrO_2 nanocomposite heterostructures, *Mater. Sci. Eng., B*, 193, 137–145.
[23] Akpan, U.G., and Hameed, B.H., 2009, Parameters affecting the photocatalytic degradation of dyes using TiO_2-based photocatalysts: A review, *J. Hazard. Mater.*, 170 (2-3), 520–529.
[24] Bafaqeer, A., Amin, N.A.S., Tahir, M., Ummer, A.C., Thabit, H.A., Theravalappil, R., Usman, J., and Ahmad, N., 2024, Construction of glucose precursor carbon/TiO_2 heterojunction with high ligand-to-metal charge transfer (LMCT) for visible light driven CO_2 reduction, *Chem. Eng. Res. Des.*, 201, 353–361.
[25] Kavetskyy, T., Smutok, O., Demkiv, O., Kukhazh, Y., Stasyuk, N., Leonenko, E., Kiv, A., Kobayashi, Y., Kinomura, A., Šauša, O., Gonchar, M., and Katz, E., 2022, Improvement of laccase biosensor characteristics using sulfur-doped TiO_2 nanoparticles, *Bioelectrochemistry*, 147, 108215.
[26] Sulaikhah, E.F., Kurniawan, R., Pradipta, M.F., Trisunaryanti, W., and Syoufian, A., 2020, Cobalt doping on zirconium titanate as a potential photocatalyst with visible-light-response, *Indones. J. Chem.*, 20 (4), 911–918.
[27] Ruzimuradov, O., Musaev, K., Mamatkulov, S., Butanov, K., Gonzalo-Juan, I., Khoroshko, L., Turapov, N., Nurmanov, S., Razzokov, J., Borisenko, V., and Riedel, R., 2023, Structural and optical properties of sol-gel synthesized TiO_2 nanocrystals: Effect of Ni and Cr (co)doping, *Opt. Mater.*, 143, 114203.
[28] Esfandian, H., Mirzaei, S., Chari, A.S., Ghadi, R.A., and Moqadam, I.H., 2024, Photocatalytic degradation of chlorpyrifos pesticide in aqueous solution using Cu-doped TiO_2/GO photocatalysis vicinity of UV and visible light, *Mater. Sci. Eng., B*, 305, 117385.
[29] Meftahi, M., Jafari, S.H., and Habibi-Rezaei, M., 2023, Fabrication of Mo-doped TiO_2 nanotube arrays photocatalysts: The effect of Mo dopant addition time to an aqueous electrolyte on the structure and photocatalytic activity, *Ceram. Int.*, 49 (7), 11411–11422.

[30] Alifi, A., Kurniawan, R., and Syoufian, A., 2020, Zinc-doped titania embedded on the surface of zirconia: A potential visible-responsive photocatalyst material, *Indones. J. Chem.*, 20 (6), 1374–1381.
[31] Li, P., Zheng, D., Gao, M., Zuo, X., Sun, L., Zhou, Q., and Lin, J., 2021, Bimetallic MOF-templated fabrication of porous Zn, N co-doped Mo_2C for an efficient hydrogen evolution reaction, *ACS Appl. Energy Mater.*, 4 (9), 8875–8882.
[32] Mittal, A., Mari, B., Sharma, S., Kumari, V., Maken, S., Kumari, K., and Kumar, N., 2019, Non-metal modified TiO_2: A step towards visible light photocatalysis, *J. Mater. Sci. Mater. Electron.*, 30 (4), 3186–3207.
[33] Yaacob, N., Sean, G.P., Mohd Nazri, N.A., Ismail, A.F., Zainol Abidin, M.N., and Subramaniam, M.N., 2021, Simultaneous oily wastewater adsorption and photodegradation by ZrO_2–TiO_2 heterojunction photocatalysts, *J. Water Process. Eng.*, 39, 101644.
[34] Jeong, W.H., Lee, H.E., Ryu, M.W., Kim, K., Kim, Y.D., and Seo, H.O., 2024, Phenol degradation on the surface of mesoporous TiO_2 particles via ligand-to-metal charge transfer under visible light irradiation, *Chem. Phys. Lett.*, 840, 141162.
[35] Khan, S., Kim, J., Sotto, A., and Van der Bruggen, B., 2015, Humic acid fouling in a submerged photocatalytic membrane reactor with binary TiO_2–ZrO_2 particles, *J. Ind. Eng. Chem.*, 21, 779–786.
[36] Długosz, O., Szostak, K., and Banach, M., 2020, Photocatalytic properties of zirconium oxide–zinc oxide nanoparticles synthesised using microwave irradiation, *Appl. Nanosci.*, 10 (3), 941–954.
[37] Li, Y., Lin, J., and Wang, G., 2019, La_2O_3/Fe_2O_3-CeO_2 composite oxide catalyst and its performance, *Adv. Mater. Phys. Chem.*, 9 (12), 219–233.
[38] Suman, S., Singh, S., Ankita, A., Kumar, A., Kataria, N., Kumar, S., and Kumar, P., 2021, Photocatalytic activity of α-Fe_2O_3@CeO_2 and CeO_2@α-Fe_2O_3 core-shell nanoparticles for degradation of Rose Bengal dye, *J. Environ. Chem. Eng.*, 9 (5), 106266.
[39] Arafati, A., Borhani, E., Nourbakhsh, S.M.S., and Abdoos, H., 2019, Synthesis and characterization of tetragonal/monoclinic mixed phases nanozirconia powders, *Ceram. Int.*, 45 (10), 12975–12982.
[40] Zhang, H., Wang, D., Han, Y., Tang, Q., Wu, H., and Mao, N., 2018, High photoactivity rutile-type TiO_2 particles co-doped with multiple elements under visible light irradiation, *Mater. Res. Express*, 5 (10), 105015.
[41] Syoufian, A., and Kurniawan, R., 2023, Visible-light-induced photodegradation of methylene blue using Mn,N-codoped $ZrTiO_4$ as photocatalyst, *Indones. J. Chem.*, 23 (3), 661–670.
[42] Bashirom, N., Tan, W.K., Kawamura, G., Matsuda, A., and Lockman, Z., 2022, Formation of self-organized ZrO_2–TiO_2 and $ZrTiO_4$–TiO_2 nanotube arrays by anodization of Ti–40Zr foil for Cr(VI) removal, *J. Mater. Res. Technol.*, 19, 2991–3003.
[43] Yodsomnuk, P., Junjeam, K., and Termtanun, M., 2018, Photoactivity of Fe and Zn-doped TiO_2 in phenol degradation under visible light, *MATEC Web Conf.*, 192, 03047.
[44] Moustafa, M., Wasnick, A., Janowitz, C., and Manzke, R., 2017, Temperature shift of the absorption edge and urbach tail of ZrS_xSe_{2-x} single crystals, *Phys. Rev. B*, 95 (24), 245207.
[45] Hao, D., Song, Y.X., Zhang, Y., and Fan, H.T., 2021, Nanocomposites of reduced graphene oxide with pure monoclinic-ZrO_2 and pure tetragonal-ZrO_2 for selective adsorptive removal of oxytetracycline, *Appl. Surf. Sci.*, 543, 148810.
[46] Obaidullah, M., Furusawa, T., Siddiquey, I.A., Bahadur, N.M., Sato, M., and Suzuki, N., 2018, A fast and facile microwave irradiation method for the synthesis of ZnO@ZrO_2 core-shell nanocomposites and the investigation of their optical properties, *Adv. Powder Technol.*, 29 (8), 1804–1811.
[47] Waweru, G.S., Kiprotich, S., and Waithaka, P., 2024, Effects of different Zn doping concentration on the optical and structural properties of TiO_2 nanoparticles, *Nanosci. Nanotechnol.*, 13 (1), 1–9.
[48] Andita, K.R., Kurniawan, R., and Syoufian, A., 2019, Synthesis and characterization of Cu-doped zirconium titanate as a potential visible-light

responsive photocatalyst, *Indones. J. Chem.*, 19 (3), 761–766.

[49] Afonso, C., Segundo, I.R., Lima, O., Landi, S., Homem, N., Costa, M.F.M., Freitas, E., and Carneiro, J., 2022, Optical, structural, morphological and chemical properties of doped TiO_2 nanoparticles with $FeCl_3$, *J. Phys.: Conf. Ser.*, 2407 (1), 012001.

[50] Lhimr, S., Bouhlassa, S., and Ammary, B., 2021, Influence of calcination temperature on size, morphology and optical properties of ZnO/C composite synthesized by a colloidal method, *Indones. J. Chem.*, 21 (3), 537–545.

[51] Hamad, H., Bailón-García, E., Pérez-Cadenas, A.F., Maldonado-Hódar, F.J., and Carrasco-Marín, F., 2020, ZrO_2-TiO_2/carbon core-shell composites as highly efficient solar-driven photo-catalysts: An approach for removal of hazardous water pollutants, *J. Environ. Chem. Eng.*, 8 (5), 104350.

[52] Guerrero-Araque, D., Ramírez-Ortega, D., Acevedo-Peña, P., Tzompantzi, F., Calderón, H.A., and Gómez, R., 2017, Interfacial charge-transfer process across ZrO_2-TiO_2 heterojunction and its impact on photocatalytic activity, *J. Photochem. Photobiol., A*, 335, 276–286.

[53] Aware, D.V., and Jadhav, S.S., 2016, Synthesis, characterization and photocatalytic applications of Zn-doped TiO_2 nanoparticles by sol–gel method, *Appl. Nanosci.*, 6 (7), 965–972.

[54] Liu, H., Su, Y., Hu, H., Cao, W., and Chen, Z., 2013, An ionic liquid route to prepare mesoporous ZrO_2–TiO_2 nanocomposites and study on their photocatalytic activities, *Adv. Powder Technol.*, 24 (3), 683–688.

[55] Fu, N., Chen, H., Chen, R., Ding, S., and Ren, X., 2023, Effect of calcination temperature on the structure, crystallinity, and photocatalytic activity of core-shell SiO_2@TiO_2 and mesoporous hollow TiO_2 composites, *Coatings*, 13 (5), 852.

[56] Vasiljević, Z., Dojčinović, M.P., Vujančević, J.D., Spreitzer, M., Kovač, J., Bartolić, D., Marković, S., Janković-Častvan, I., Tadić, N.B., and Nikolić, M.V., 2021, Exploring the impact of calcination parameters on the crystal structure, morphology, and optical properties of electrospun Fe_2TiO_5 nanofibers, *RSC Adv.*, 11 (51), 32358–32368.

[57] Kayani, Z.N., Saleemi, F., and Batool, I., 2015, Effect of calcination temperature on the properties of ZnO nanoparticles, *Appl. Phys. A*, 119 (2), 713–720.

[58] Padmamalini, N., and Ambujam, K., 2016, Structural and dielectric properties of ZrO_2–TiO_2–V_2O_5 nanocomposite prepared by CO-precipitation calcination method, *Mater. Sci. Semicond. Process.*, 41, 246–251.

[59] Gaber, A.A., Abd El-Hamid, H.K., Ngida, R.E.A., Sadek, H.E.H., and Khattab, R.M., 2024, Synthesis, characterization and corrosive resistance of ZnO and ZrO_2 coated TiO_2 substrate prepared via polymeric method and microwave combustion, *Ceram. Int.*, 50 (20, Part B), 38917–38932.

[60] Aguirre-Cortés, J.M., Munguía-Ubierna, Á., Moral-Rodríguez, A., Pérez-Cadenas, A.F., Carrasco-Marín, F., and Bailón-García, E., 2024, Size-miniaturization of TiO_2-ZrO_2 coupled semiconductors to develop highly efficient visible-driven photocatalysts for the degradation of drugs in wastewater, *Appl. Surf. Sci.*, 670, 160609.

[61] Sakfali, J., Ben Chaabene, S., Akkari, R., Dappozze, F., Berhault, G., Guillard, C., and Saïd Zina, M., 2022, High photocatalytic activity of aerogel tetragonal and monoclinic ZrO_2 samples, *J. Photochem. Photobiol., A*, 430, 113970.

[62] Thakur, S., Sareen, S., Verma, M., Kaur, K., and Mutreja, V., 2024, Synthesis of elusive monoclinic ZrO_2 nanostructures via hydrothermal treatment, *J. Inorg. Organomet. Polym. Mater.*, 34 (1), 61–78.

[63] Shishodia, G., Gupta, S., Pahwa, N., and Shishodia, P.K., 2024, ZrO_2 nanoparticles synthesized by the sol–gel method: Dependence of size on pH and annealing temperature, *J. Electron. Mater.*, 53 (9), 5159–5168.

[64] Muslim, M.I., Kurniawan, R., Pradipta, M.F., Trisunaryanti, W., and Syoufian, A., 2021, The effects of manganese dopant content and calcination temperature on properties of titania-zirconia composite, *Indones. J. Chem.*, 21 (4), 882–890.

[65] Muzammil, P., Basha, S.M., and Muhammed, G.S.,

2020, Structural and magnetic properties of Fe-doped GaN by sol-gel technique, *J. Supercond. Novel Magn.*, 33 (9), 2767–2771.

[66] Huang, K., Chen, L., Xiong, J., and Liao, M., 2012, Preparation and characterization of visible-light-activated Fe-N co-doped TiO_2 and its photocatalytic inactivation effect on leukemia tumors, *Int. J. Photoenergy*, 2012 (1), 631435.

[67] Jaiswal, R., Bharambe, J., Patel, N., Dashora, A., Kothari, D.C., and Miotello, A., 2015, Copper and nitrogen co-doped TiO_2 photocatalyst with enhanced optical absorption and catalytic activity, *Appl. Catal., B*, 168-169, 333–341.

[68] RamezaniSani, S., Rajabi, M., and Mohseni, F., 2020, Influence of nitrogen doping on visible light photocatalytic activity of TiO_2 nanowires with anatase-rutile junction, *Chem. Phys. Lett.*, 744, 137217.

[69] Kurniawan, R., Sudiono, S., Trisunaryanti, W., and Syoufian, A., 2019, Synthesis of iron-doped zirconium titanate as a potential visible-light responsive photocatalyst, *Indones. J. Chem.*, 19 (2), 454–460.

[70] Syoufian, A., and Kurniawan, R., 2024, Codoping of nickel and nitrogen in ZrO_2-TiO_2 composite as photocatalyst for methylene blue degradation under visible light irradiation, *Indones. J. Chem.*, 24 (4), 1218–1227.

[71] Emeline, A.V., Zhang, X., Murakami, T., and Fujishima, A., 2012, Activity and selectivity of photocatalysts in photodegradation of phenols, *J. Hazard. Mater.*, 211-212, 154–160.